PHYSICAL REVIEW APPLIED **19,** 024034 (2023)

Field-Free Current-Induced Switching of $L1_0$-FePt Using Interlayer Exchange Coupling for Neuromorphic Computing

Kaifeng Dong,[1,2,3] Zhe Guo,[4,*] YiYi Jiao,[1,2,3] Ruofan Li,[4] Chao Sun,[1,2,3] Ying Tao,[1,2,3] Shuai Zhang,[4]
Jeongmin Hong,[4] and Long You[4,†]

[1] *School of Automation, China University of Geosciences, Wuhan 430074, China*
[2] *Hubei Key Laboratory of Advanced Control and Intelligent Automation for Complex Systems, Wuhan 430074, China*
[3] *Engineering Research Center of Intelligent Technology for Geo-Exploration, Ministry of Education, Wuhan 430074, China*
[4] *School of Optical and Electronic Information and Wuhan National Laboratory for Optoelectronics, Huazhong University of Science and Technology, Wuhan 430074, China*

(Received 8 July 2022; revised 14 October 2022; accepted 13 January 2023; published 13 February 2023)

$L1_0$-phase FePt is well known for its unusually robust perpendicular magnetic anisotropy (PMA) properties arising from strong conduction-electron spin-orbit coupling (SOC) with the Fe orbital moment. The strong PMA enables stable magnetic storage and memory devices with ultrahigh capacity. Meanwhile, SOC is also the premise of the recently discovered spin-orbit-torque (SOT) effect, which opens avenues for possible electrical manipulation of magnetization for $L1_0$-FePt. The bulk SOT of the $L1_0$-FePt single layer was discovered recently; this leads to the magnetization of $L1_0$-FePt reversibly switching on itself. However, deterministic SOT switching of bulk perpendicularly magnetized FePt magnets relies on an external magnetic field to break the symmetry. Here, the symmetry-breaking issue is resolved by interlayer exchange coupling, where the FePt layer is coupled with an in-plane magnetized NiFe layer through a TiN spacer layer. Furthermore, our device also presents memristive or gradual switching behaviors, even without an external field, offering the potential for constructing spin synapses and spin neurons for neuromorphic computing. An artificial neural network with high accuracy (~91.17%) is realized based on the constructed synapses and neurons. Our work paves the way for field-free SOT switching of single bulk PMA magnets and their potential applications in neuromorphic computing.

DOI: 10.1103/PhysRevApplied.19.024034

I. INTRODUCTION

The demand for high-density and energy-efficient nonvolatile memory has increased drastically over the past half-century, as the market for consumer electronics has expanded. Spin-orbit-torque (SOT) magnetic random-access memory (MRAM) using a magnetic material with perpendicular magnetic anisotropy (PMA) is one of the most promising nonvolatile memory technologies, as it combines advantages such as quasi-infinite write endurance, high speed, and scalability [1–9].

To date, most studies on SOT in PMA materials has focused on the heavy-metal (HM)/ferromagnet (FM) structure with interfacial PMA [1,2]. However, magnets with interfacial PMA, which requires the FM layer to be ultrathin, cannot be scaled down to less than 20 nm, even using a double interface, since the effective perpendicular anisotropy energy dominated by interfacial anisotropy reaches the physical limit of providing sufficient thermal stability [10]. Alternatively, FM/FM multilayers, such as Co/Ni, can be grown very thick while retaining their PMA [11,12]. However, the strength of SOT scales inversely with the thickness of a FM layer [2]. Therefore, the remaining challenges of perpendicular SOT MRAM include the relatively high current density of spin-torque switching and the low thermal stability of the bit cell. Nevertheless, it is demonstrated that an electric current can exert a large spin torque on $L1_0$-FePt magnets, which possess inherent superior perpendicular magnetocrystalline anisotropy, ultimately achieving reversible magnetization that switches on itself [13–15]. Remarkably, the current-induced spin torque and the quantified effective magnetic fields monotonically increase with increasing film thickness, exhibiting a bulk characteristic. Thus, the bulk spin torque observed in a single layer of $L1_0$-FePt shows great potential for removing those remaining obstacles in perpendicular SOT MRAM and brings perspectives for SOT research and applications.

---

[*] guozhe@hust.edu.cn
[†] lyou@hust.edu.cn

For perpendicularly magnetized layers, however, an extra in-plane magnetic field is indeed required to break symmetry for deterministic switching, but it is impractical to generate the field externally for spintronic applications. To date, a variety of field-free approaches have been demonstrated, such as a wedged structure [16,17], exchange bias [18], electric field control [19], and stray fields [20]. As a potentially scalable way, interlayer exchange coupling (IEC), where two FM layers are coupled through a nonmagnetic (NM) spacer layer, is widely adopted to realize field-free switching in an interfacial PMA structure and CoPt alloy film, with low magnetic anisotropy [21–24].

Here, we demonstrate field-free current-induced switching of $L1_0$-FePt utilizing IEC. We fabricate a MgO/FePt/TiN/NiFe film stack, where the perpendicularly magnetized FePt layer is coupled with an in-plane NiFe layer through the TiN spacer. With two different thicknesses of spacer layer, the FM and antiferromagnetic (AFM) couplings are observed. Both cases present reversible SOT switching without an external field, but the switching polarities of the two devices are opposite in sign due to opposite IEC. Furthermore, we find that in our device the resistance states can be controlled continuously through adjusting the counts of applied current pulses, even in the absence of external fields, exhibiting memristive behavior. Therefore, we believe that our work paves the way for developing ultrahigh-density MRAM and its neuromorphic computing applications.

II. EXPERIMENTS

A. Sample preparation

The FePt film is deposited onto (001)MgO substrate using dc magnetron sputtering from a FePt alloy target at a base pressure less than 9×10^{-8} Torr. The sputtering power is 50 W and the substrate temperature during deposition is kept at 600 °C. The as-deposited film is *in situ* annealed at 600 °C for 0.5 h. The TiN and NiFe layers are deposited from single TiN and NiFe targets, respectively. The TiN and NiFe films are both grown with a power of 100 W and temperature of 600 °C. The deposition pressure is kept at 3 mTorr for all the layers. After film deposition, the sample is patterned into a Hall bar structure using photolithography and ion milling.

B. Sample characterization

The crystal structure is characterized by x-ray diffraction (XRD) with a Bruker AXS D8-Focus instrument. Scanning transmission electron microscopy (TEM) high-angle annular dark field (HAADF) imaging is performed using an FEI TitanThemis 200 TEM instrument. Cross-section TEM samples are prepared by using a focused-ion-beam machine (FEI Helios 450S dual-beam FIB). The composition of the films is analyzed by energy-dispersive x-ray spectroscopy (EDS) with a Bruker super-X EDS instrument. The thickness of films is extracted from the TEM image.

C. Current-induced-switching measurements

Current-driven magnetization switching is performed through detecting the anomalous Hall resistance, while sweeping the dc current pulse. Writhing current pulses with varying amplitudes are applied to the Hall bar channel with a duration of 5 ms using a Keithley 6221 source meter. Then a reading current pulse of 0.1 mA with a duration of 5 ms is applied to measure the Hall voltage using a Keithley 2182A nanovoltmeter.

D. Harmonic measurements

The device is first magnetized to a saturated state by applying a large field (±1 T) perpendicular to the film plane. A 317.3-Hz frequency ac current is applied to the Hall bar channel. The first- and second-harmonic Hall voltages are simultaneously collected by two Stanford SR830 lock-in amplifiers, while the magnetic field is applied either along or orthogonal to the current-flow direction. A uniform current density is assumed throughout the heterostructure.

III. RESULTS AND DISCUSSION

A. Characterization of FePt and current-induced SOT switching of single FePt layers

The FePt film (5 nm) with 2-nm TiN as a capping layer is deposited onto (001)MgO. The inset of Fig. 1(a) shows the crystal structure of $L1_0$-FePt, where Fe and Pt atomic layers are alternately stacked along the c axis. The XRD pattern of the sample [Fig. 1(a)] confirms the $L1_0$ phase. We then pattern the film into a Hall bar structure with a width of 6 μm for transport measurement [Fig. 1(b)]. The anomalous Hall effect (AHE) tests are performed under out-of-plane field H_z and the AHE loop in Fig. 1(c) shows that the deposited FePt film has a good PMA.

First, we investigate the current-induced-switching performance of a single FePt layer. The current-induced magnetization switching is conducted through applying current pulses with varying magnitudes along the x axis [Fig. 1(b)], while the Hall resistances (R_H) are collected with a smaller reading current after each writing pulse. Figure 1(d) shows the switching loops under different in-plane fields (H_x), which vary from 200 to −200 Oe. One can clearly observe the hysteresis switching loops, except when $H_x = 0$ Oe. Moreover, the switching polarities (clockwise or anticlockwise) change with the reversal of H_x, presenting similar behavior to the SOT switching in the HM/FM structure and other previous studies on

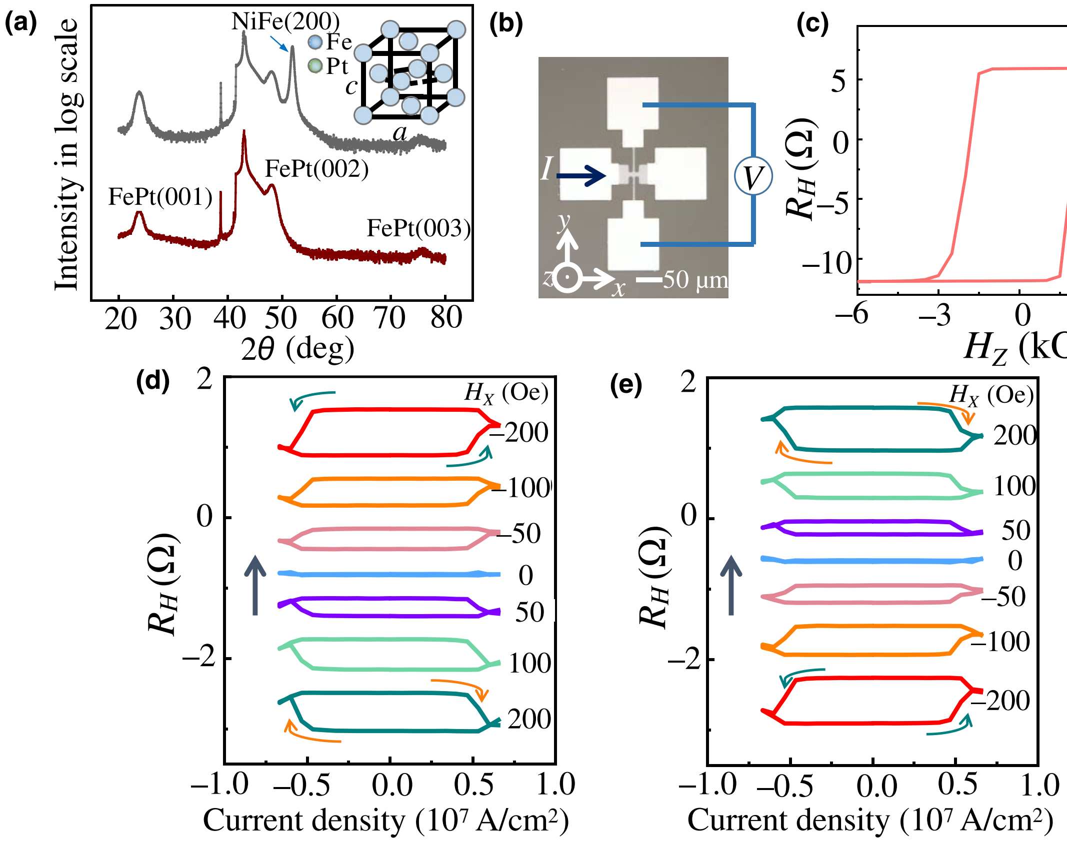

FIG. 1. $L1_0$-phase FePt and its current-induced switching. (a) XRD pattern of MgO (substrate)/FePt (gray line) and FePt/TiN/NiFe heterostructure (dark-red line). Inset shows a schematic of the crystal structure of $L1_0$-FePt. (b) Optical top-view image of the fabricated Hall bar device, and schematic of the current-induced-switching measurement setup. (c) AHE loop showing PMA of the FePt layer. Current-induced magnetization switching of FePt layer under different in-plane fields, which range from 200 to −200 Oe (d) and −200 to 200 Oe (e). Gray arrows indicate the sequence of applied in-plane fields. H_x and H_z represent the applied magnetic field along x and z axes, respectively.

FePt [13,14]. When H_x changes from −200 to 200 Oe, the switching loops [Fig. 1(e)] are similar as the ones shown in Fig. 1(d), indicating that the single-layer switching process is independent of the application sequence of H_x. In addition, under low temperature (100 K), the switching has also been observed (Fig. S1 within the Supplemental Material [25]).

B. Field-free SOT switching using IEC

Next, we utilize IEC to realize the field-free switching of the $L1_0$-FePt layer. A quantitative description of IEC can be phenomenologically expressed as $E = -J_1 \cos(\Delta\varphi) - J_2 \cos^2(\Delta\varphi)$, where E is the interlayer-coupling areal energy density; $\Delta\phi$ is the angle between magnetization of two layers; and parameters J_1 and J_2 represent the strengths of bilinear and biquadratic coupling, respectively [26]. As reported, J_2 is very small and can be considered negligible for perfect layered systems; it is usually affected by extrinsic effects [27]. J_1 oscillates with the thickness of the NM spacer layer. If J_1 is positive, magnetization of the two layers prefers to be along the same direction. In contrast, when J_1 is negative, magnetization tends to be oppositely aligned. Therefore, the IEC strength oscillates with the thickness of the NM spacer layer, where the two FM layers are alternatingly antiferromagnetically or ferromagnetically coupled. Here, a FePt/TiN/NiFe trilayer structure is employed for IEC, in which the NiFe layer has an in-plane magnetization. Figure 2(a) displays the HAADF cross-section image of one sample and its corresponding EDS mapping, showing distinct interfaces between different layers. The XRD pattern of the heterostructure shows that the grown NiFe film has an in-plane crystal structure [Fig. 1(a), black line]. Our previous work indicated that the grown NiFe film preferred in-plane magnetization due to shape anisotropy and had a high remanence ratio close to one [28]. Specifically, we fabricate two stacks with different TiN thicknesses, which are FePt(5)/TiN(2.3)/NiFe(15) (stack 1, numbers indicate the thickness in nm) and FePt(5)/TiN(3.5)/NiFe(15) (stack 2). Interestingly, AFM and FM couplings are, respectively, observed in these two stacks. It is noted that the fabricated

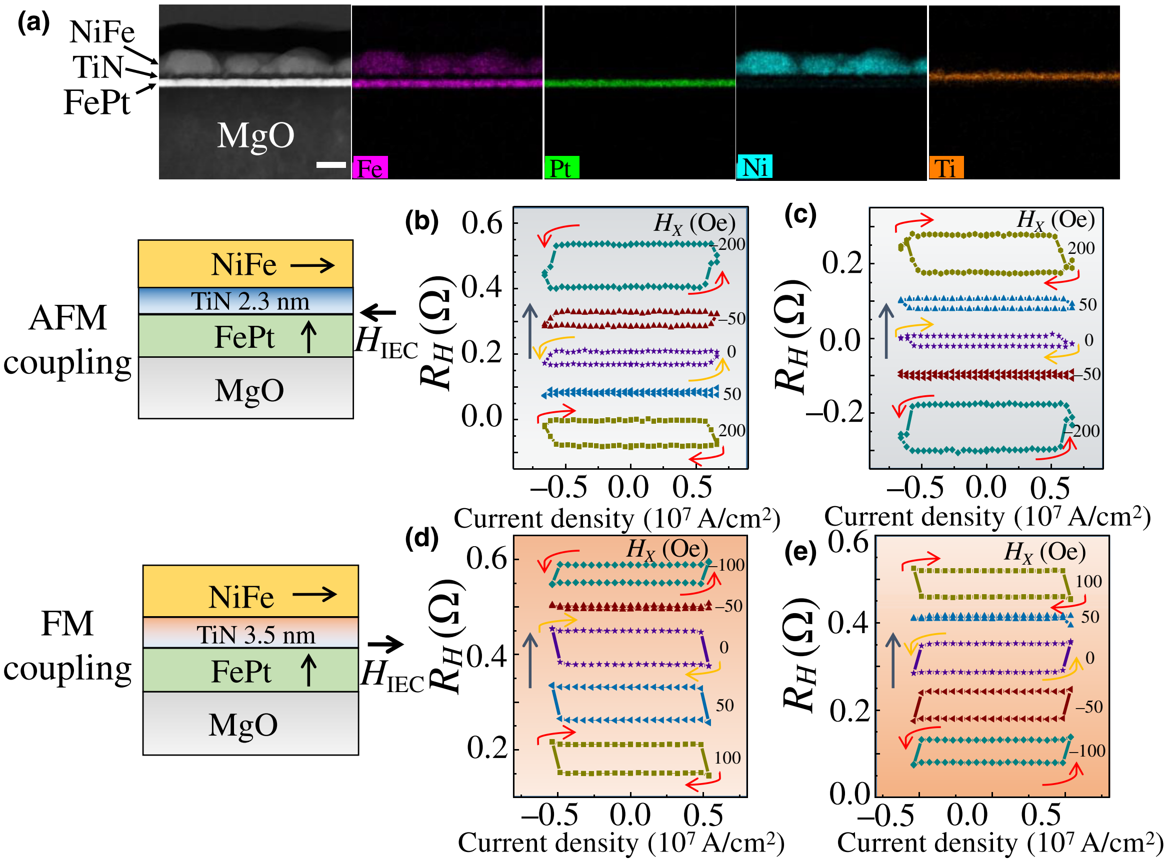

FIG. 2. Field-free switching with different IEC couplings. (a) HAADF image of the FePt(5)/TiN(3.5)/NiFe(15) sample and its corresponding EDS mapping. Scale bar is 10 nm. (b),(c) Current-induced-switching process for the stack of FePt(5)/TiN(2.3)/NiFe(15) with different sequences of applied H_x, which are indicated by gray arrows. Field-free switching is observed and the switching polarities at $H_x = 0$ Oe are opposite to that at $H_x = 200$ Oe in (b) or $H_x = -200$ Oe in (c), exhibiting AFM coupling. (d),(e) Current-induced-switching process for the stack of FePt(5)/TiN(3.5)/NiFe(15), where FM couplings are observed. Note that (b)–(e) are the corrected switching loops after considering shunting effects (see Supplemental Material Note 1 [25]).

Hall bar structure for field-free switching has a width of 15 µm.

Figures 2(b) and 2(c) show the current-induced switching of stack 1 collected at various external applied fields H_x but with the opposite applied sequence of H_x; the gray arrows indicate the sequence of measurement. Both Figs. 2(b) and 2(c) exhibit deterministic switching in the absence of an external field, while opposite signs (clockwise or anticlockwise) of current-induced magnetization switching are observed at 0 Oe. In Fig. 2(b), with H_x varying from 200 to −200 Oe, the switching loops are reversed at $H_x = 50$ Oe. We can see the switching polarity at $H_x = 0$ Oe is opposite to the one of $H_x = 200$ Oe. We interpret this using an IEC-induced effective field, H_{IEC} [21,22], acting on the bottom FePt layer coming from interlayer coupling. At a high H_x (200 Oe), the NiFe layer is saturated and the induced H_{IEC} is opposite to the direction of H_x, which represents an AFM coupling. With H_x decreasing to 50 Oe, the switching loop is not observed due to the weak total effective field; in other words, the external field, H_x, is counteracted by H_{IEC}. Thus, $|H_{IEC}|$ is determined to be about 50 Oe here. At $H_x = 0$ Oe, the existence of H_{IEC} breaks the symmetry, and consequently, field-free deterministic switching is obtained. In contrast, when H_x changes from −200 to 200 Oe, the symmetric variation trends are observed [Fig. 2(c)]. The reversal of the switching loop occurs at $H_x = -50$ Oe, confirming that the magnitude of H_{IEC} in such a structure is about 50 Oe. Figures 2(d) and 2(e) show the switching of stack 2 with H_x changing from 100 to −100 Oe and −100 to 100 Oe, respectively. Field-free switching is also obtained in stack 2, whereas FM coupling is observed in such a stack, in which the induced H_{IEC} has the same direction as the magnetization of the NiFe layer. Different from stack 1, the change of switching polarity occurs when H_x is reversed. We have therefore realized zero-field switching of $L1_0$-FePt magnets. Different thicknesses of the TiN spacer layer cause opposite couplings between FePt and NiFe layers, which is a typical attribute of IEC [29].

C. Quantitative evaluation of the SOT effective field

To predict the current-induced effective magnetic fields during switching, we also perform harmonic Hall voltage measurements. An ac current signal with a frequency of 317.3 Hz is applied, as schematically shown in Fig. 3(a). The external in-plane magnetic fields are applied along the transverse or longitudinal directions; these are employed to analyze the transverse (H_T) or longitudinal (H_L) effective fields, respectively. Both the first- (V_ω) and second- ($V_{2\omega}$) harmonic Hall voltages are collected simultaneously. $H_{L(T)}$ can be calculated through [30]

$$\Delta H_{L(T)} = -2\frac{B_{L(T)} \pm 2\xi B_{T(L)}}{1-4\xi^2},$$

where ξ is the ratio between the planar and anomalous Hall resistances (Fig. S2 within the Supplemental Material [25]) and $\pm$ denotes the upward or downward magnetization directions; $B_{L(T)}$ is defined as $\{(\partial V_{2\omega}/\partial H)/(\partial^2 V_\omega/\partial H^2)\}_{H//L(T)}$. The thermal effect is also considered in the harmonic measurements (see Supplemental Material Note 2 [25]).

Figure 3(b) shows the V_ω and $V_{2\omega}$ measurement results as a function of longitudinal (H_x) or transverse (H_y) fields for the FePt(5)/TiN(2.3)/NiFe(15) stack on MgO substrate. The V_ω variations approximate quadratic curves. Under different magnetization directions, $V_{2\omega}$ as a function of H_x shows a consistent variation trend, while the ones as a function of H_y present the opposite symmetry. Harmonic measurements of the FePt(5)/TiN(3.5)/NiFe(15) stack and a single FePt layer also exhibit the same variation trends (Figs. S3 and S4 within the Supplemental Material [25]). These phenomena are similar to the SOT switching observed in the HM/FM structure with interfacial PMA. The calculated $\Delta H_{L(T)}$ values as a function of current density are shown in Fig. 3(c), where ΔH_L is much larger than ΔH_T for each stack. In addition, the extracted spin-torque efficiency, $\beta_{L(T)}$, of two stacks, i.e., FePt(5)/TiN(2.3or3.5)/NiFe(15), which is defined as $\Delta H_{L(T)}/j$, is nearly consistent. The β_L values of stacks 1 and 2 are 108.9 and 117.7 Oe/(10^7 A/cm^2), while β_T are 33.8 and 34.5 Oe/(10^7 A/cm^2), respectively. This means that the different exchange couplings do not alter the spin-orbit efficiency of FePt magnets; this also reflects their bulk characteristic.

D. Memristive switching for artificial synapses

In addition to magnetization flipping between binary states for digital memory, as discussed above, we also find that the magnetization of $L1_0$-FePt changes in an analog manner with a string of electric current pulses, which could be used as a synapse for neuromorphic computing [31–35]. As a fundamental unit of an artificial neural network, the artificial synapse is responsible for the connectivity between two neurons and updates the connection strength

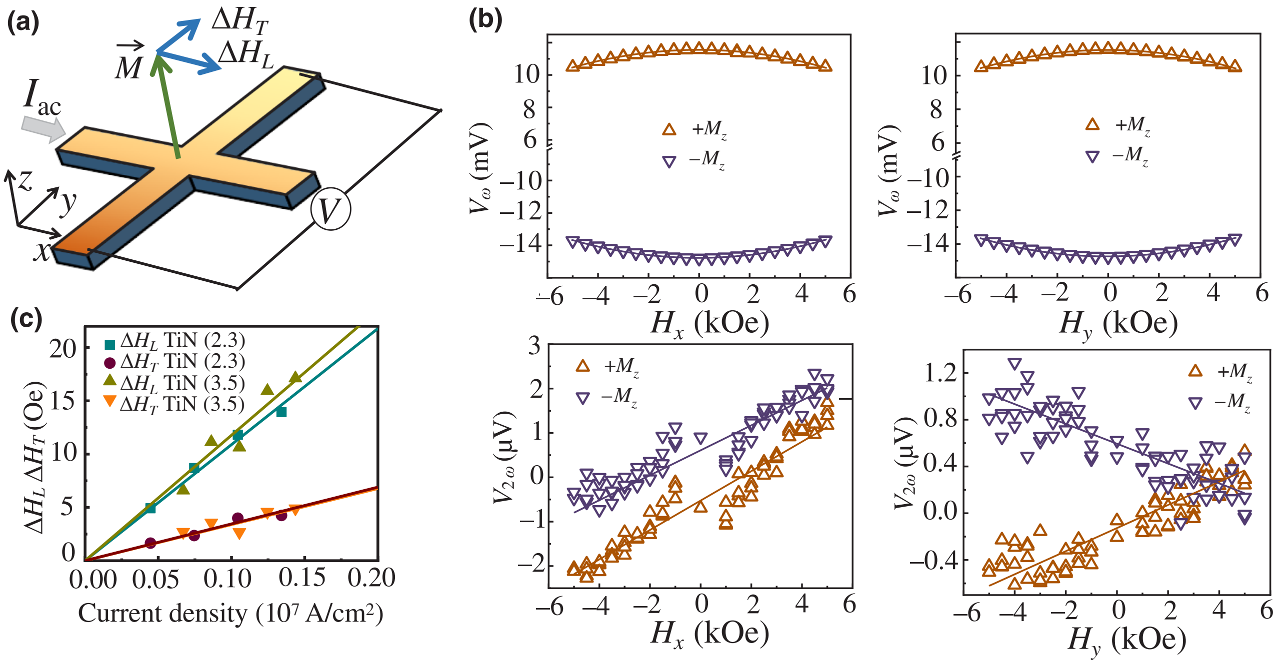

FIG. 3. Evaluation of the spin-orbit effective fields. (a) Schematic of spin-orbit effective fields and the setup for harmonic measurement. (b) Field dependence of first- and second-harmonic signals for the FePt(5)/TiN(2.3)/NiFe(15) heterostructure. Up and down triangular symbols correspond to $+M_z$ and $-M_z$ of the FePt layer, respectively. (c) Current-density dependence of longitudinal and transverse spin-torque effective fields of FePt(5)/TiN(2.3)/NiFe(15) and FePt(5)/TiN(3.5)/NiFe(15).

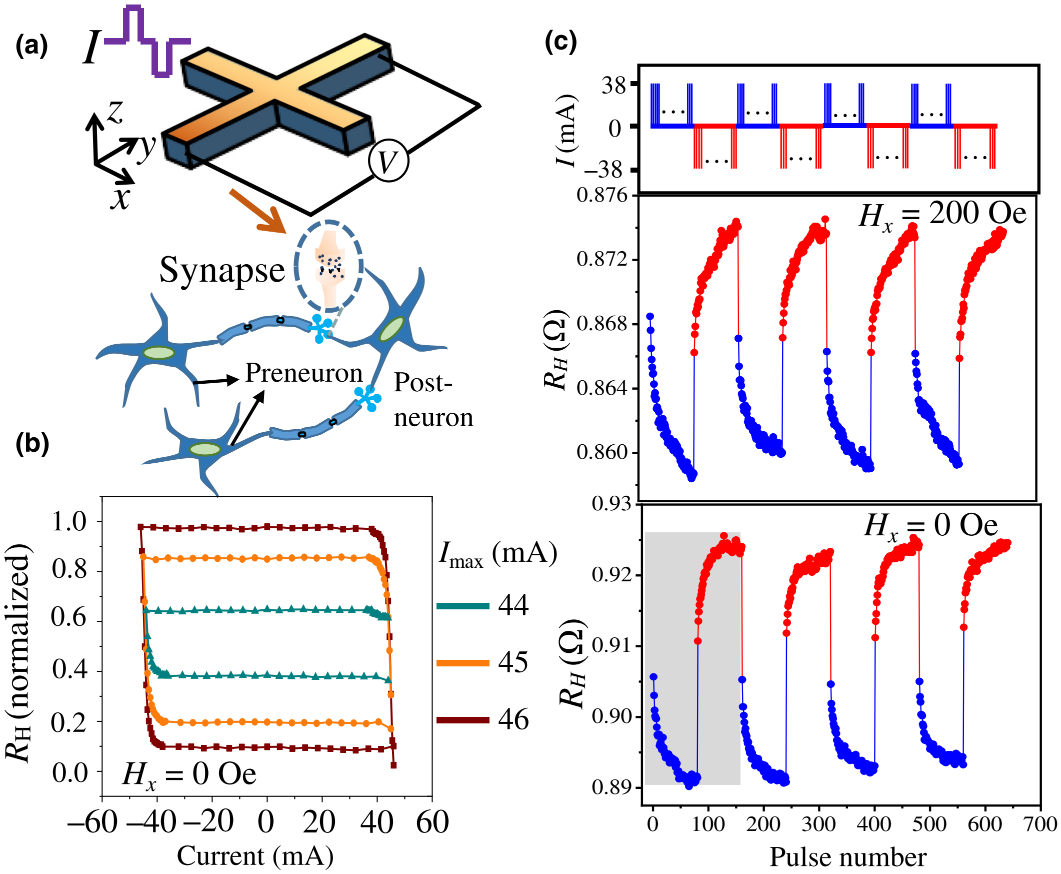

FIG. 4. Memristive switching by electrical current pulses. (a) Cartoon of a biological synapse and neuron, and the measurement setup for memristive switching. (b) R_H-I loops with varying maximum current magnitude, $I_{\max}$, under $H_x = 0$ Oe. Note that the applied maximum current value, namely, 46 mA, corresponds to the current density of 0.506×10^7 A/cm^2. (c) R_H variations tuned by programming consecutive pulse sequences. Top panel illustrates the applied current pulses for tuning R_H, where equal numbers (80) of positive (+38 mA) and negative (−38 mA) pulses are alternately applied. Each pulse has a duration of 50 µs. Middle and bottom panels show R_H variations under current pulses with $H_x = 200$ and 0 Oe, respectively.

via its weight [Fig. 4(a)], the conductance of which should be modulated continuously and be nonvolatile.

As shown in Fig. 4(b), we vary the maximal magnitude of the applied current from 44 to 46 mA at zero external field using the FM coupling sample and a series of hysteretic loops are observed. One can find that the final resistance states can effectively be determined by the current cycle protocol, showing the memristive switching characteristic. Moreover, the resistance variations tuned by programming consecutive pulse sequences are desired to imitate synaptic behavior. As shown in Fig. 4(c) (top panel), a train of positive current pulses with a fixed amplitude (+38 mA) and number (80), and subsequent negative ones with a constant amplitude (−38 mA) and equal number (80), are applied along the x axis to stimulate the device. With $H_x = 200$ and 0 Oe, the response of R_H [Fig. 4(c), middle and bottom panels] demonstrates that the consecutive positive pulses lead to the gradual decrease of R_H, while negative ones cause the increase of R_H, corresponding to the depression and potentiation of the synapse, respectively. The underlying mechanism could be domain nucleation and expansion in the Hall bar device [13]. In addition, each string of positive (negative) pulses can reproducibly determine the same or similar low (high) final resistance states at the end of application. We also apply a train of current pulses, where the positive pulses have a gradually increasing number of pulses (from 50 to 70, 90, and 110), while the negative ones retain a constant number (80). As a result, the change in the number of positive pulses enables different resistance levels, and R_H gradually decreases as the number of positive pulses varies (Fig. S5 within the Supplemental Material [25]). The above synaptic plasticity demonstrates that our device can be used in self-adaptive networks with synaptic functionality.

E. A sigmoidal artificial neuron

We also use the current-induced gradual switching of $L1_0$-FePt to construct an artificial neuron

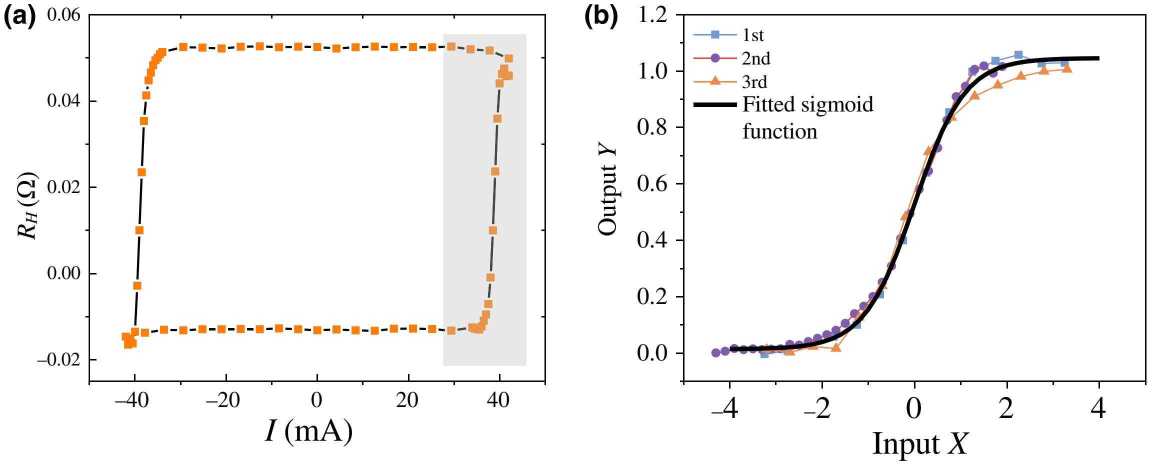

FIG. 5. Sigmoidal artificial neuron. (a) Typical field-free switching loop, where data points in the shaded area are utilized for extracting the analog sigmoid function for an artificial neuron. (b) Data points selected from three repeated switching loops are used to obtain the analog sigmoid function. Black solid line represents the analog sigmoid function.

with a sigmoid activation function [36]. Figure 5(a) shows a typical switching loop at $H_x = 0$ Oe for the FePt(5)/TiN(3.5)/NiFe(15) sample. An analog sigmoid function is built through mapping the selected R-I data points in the shaded region of Fig. 5(a) onto a sigmoid function. Based on the data points measured repeatedly three times, the fitted analog sigmoid function is plotted in Fig. 5(b) (black line). In practical applications, each input X is converted into current I that triggers the magnetization switching of $L1_0$-FePt, then the measured R_H is transformed into output Y.

F. Artificial neural network (ANN) for pattern recognition

We exploit the artificial synapse and neuron to simulate an ANN for pattern recognition. The multilayer perceptron algorithm is used to learn a handwritten dataset (three characters, “c,” “u,” and “g”), the image size of which is 28 × 28. As shown in Fig. 6(a), the network has 784, 3, and 3 neurons for the input layer, hidden layer, and output layer, respectively. The grayscale value of each pixel is converted into a one-dimensional array with a length of 784, acting as the input of the input layer. The output layer uses the SOFTMAX function to perform the three-classification output of the dataset, and the output neuron with the highest probability corresponds to the predicted label category. We use the classic gradient descent and backward propagation algorithm to perform the training process. The mean-square-error function is used as the loss function. Here, we consider three different cases. First, the fitted sigmoid function in Fig. 5(b) is used as the activation function of the hidden layer, while the ideal software-based synapse is used for weight updating, which is named as case 1. Second, the synaptic weights with 160 resistance states extracted from the experimental results [indicated by the shaded area in Fig. 4(c)] and the ideal sigmoid neuron are used for the ANN (case 2). Third, both the synapse and sigmoidal neuron are extracted from the experimental results (case 3).

For each ANN, we train 14 400 images and then test 2400 images. Figure 6(b) shows the simulated pattern-recognition accuracy as a function of training numbers; an ANN with both an ideal synapse and ideal sigmoidal artificial neurons is used for accuracy comparison. Our simulation demonstrates that the ANN based on case 1 and case 2 can reach a pattern-recognition accuracy of about 93.71% and 92.50%, respectively, which is close to the accuracy of ideal software-based training (95.04%). Case 3 achieves the lowest accuracy of 91.17%, although it still presents relatively high accuracy. Overall, our device demonstrates potential as an artificial synapse and neuron, which can be exploited to construct an ANN with high accuracy.

G. Discussion

Here, the anomalous Hall resistance is exploited to follow perpendicular magnetization switching that, however, has limited variation ratios. To improve the sensitivity, magnetoresistive read-out, such as tunnel magnetoresistance, should be introduced into the memory configuration. However, in the HM/FM structure that has interfacial PMA, the FM switching layer is sandwiched by the HM layer and spacing layer when using IEC to realize field-free switching. Thus, it is hard to construct a magnetic-tunnel-junction (MTJ) read-out unit in such a structure. One possible approach is to condense the HM layer and spacing layer into one single layer; however, this could reduce the PMA and result in weak IEC, as reported in Ref. [21]. In this regard, $L1_0$-FePt is free from this problem, since it does not need another adjacent layer to serve as the

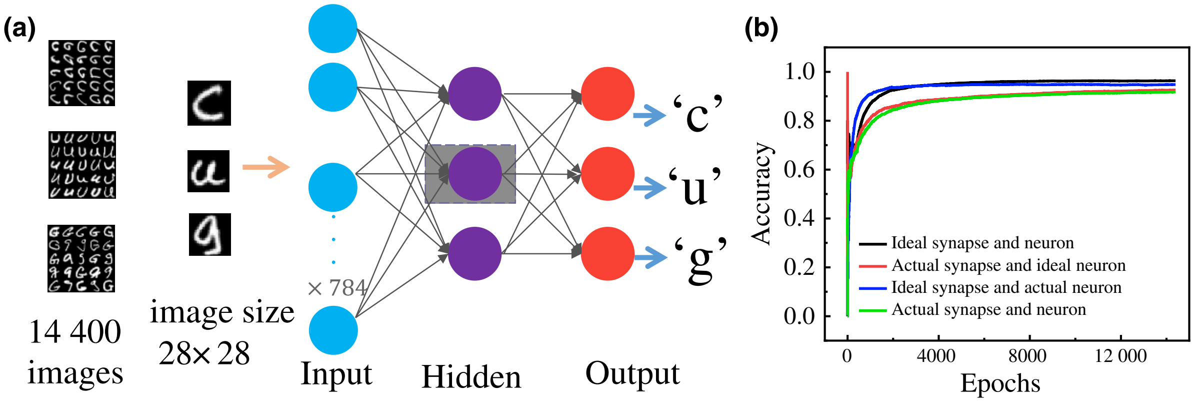

FIG. 6. ANN based on the sigmoidal artificial neuron. (a) ANN consisting of three layers, where the input layer, hidden layer, and output layer have 784, 3, and 3 neurons, respectively. Sigmoidal artificial neuron extracted from experimental results serves as the hidden-layer neuron. 14 400 and 2400 images are used for training and testing, respectively. (b) Accuracy for training 14 400 images with different combinations of synapses and neurons.

spin-torque source, thereby enabling the MTJ to be in the field-free configuration.

On the other hand, the strengths of the effective field due to IEC are also associated with the magnetic layer thickness. According to previous reports [37,38], the strengths of IEC show oscillatory behavior with respect to the magnetic layer thickness due to interference from electron Bloch waves in the ferromagnetic layers. Specifically, the amplitude of the oscillations decreases essentially as L^{-2}, where L represents the magnetic layer thickness. Accordingly, the magnetoresistance ratio using the MTJ readout structure will also decrease. It is also noted that the strengths of IEC are affected by other factors, such as the nonmagnetic-spacer-layer material and the thickness of the spacer layer. Through optimizing the spacer-layer material or adjusting the spacer-layer thickness, one can achieve a large magnetic-layer-thickness range that can be affected by IEC.

Moreover, we also notice that the current-induced switching of $L1_0$-FePt demonstrated in our work is partial switching. Such a phenomenon is also widely found in other studies [13,14]. The origin of SOT in a single FePt layer is regarded as possibly originating from the composition gradient along the film thickness [13,14]. One possible approach to increase the switching ratio is to use an artificial composition gradient [24], in which a distinct composition gradient can be formed in the FePt alloy.

IV. CONCLUSION

We demonstrate field-free current-induced switching of $L1_0$-phase FePt that has good PMA using IEC. The FePt(5 nm)/TiN/NiFe(15 nm) heterostructure is employed in our work, in which the top NiFe layer has in-plane magnetization, and TiN serves as the nonmagnetic spacing layer. With different thicknesses of TiN layer, antiferromagnetic (2.3-nm TiN) and ferromagnetic couplings (3.5-nm TiN) are both observed. Harmonic measurements indicate that the spin-torque efficiencies in these two couplings are nearly consistent, where longitudinal spin-torque efficiencies are 108.9 and 117.7 Oe/(10^7 A/cm^2) for antiferromagnetic and ferromagnetic couplings, respectively, and transverse ones are 33.8 and 34.5 Oe/(10^7 A/cm^2). In addition, the memristive switching behavior of our device is investigated, in which the device states can be programmed in an analog manner by consecutive current pulses, even without an external field. Meanwhile, a sigmoidal artificial neuron is constructed, and an ANN based on such neurons can achieve a high recognition accuracy of about 91.17%. Thus, we believe that our work paves the way for high-density MRAM and its neuromorphic applications.

ACKNOWLEDGMENTS

This work is supported by the National Natural Science Foundation of China (NSFC, Grants No. 62074063, No. 61904060, No. 61821003, and No. 61674062); the Fundamental Research Funds for the Central Universities, China University of Geosciences (Wuhan) (Grants No. CUG150632 and No. CUGL160414); the National Key Research and Development Program of China (Grant No. 2020AAA0109005); the Fundamental Research Funds for the Central Universities (HUST, Grant No. 2018 KFYXKJC019); and the Research Project of Wuhan Science and Technology Bureau (Grant No. 2019010701011394). Z.G. acknowledges support from the China Postdoctoral Science Foundation (Grants No. 2019M652642 and No. 2021T140228). K. Dong and Z. Guo contributed equally to this work. K.D. and L.Y. conceived the idea. Y.J. deposited the film. Y.J. and R.L. fabricated the devices. Z.G., Y.J., C.S., and S.Z. performed the electrical and magnetic property measurements. Y.J.

conducted the TEM characterization. Z.G., K.D., and L.Y. wrote the manuscript. All authors commented on the manuscript.

[1] C. Song, R. Zhang, L. Liao, Y. Zhou, X. Zhou, R. Chen, Y. You, X. Chen, and F. Pan, Spin-orbit torques: Materials, mechanisms, performances, and potential applications, Prog. Mater. Sci. **118**, 100761 (2021).

[2] R. Ramaswamy, J. M. Lee, K. Cai, and H. Yang, Recent advances in spin-orbit torques: Moving towards device applications, Appl. Phys. Rev. **5**, 031107 (2018).

[3] L. Liu, C.-F. Pai, Y. Li, H. W. Tseng, D. C. Ralph, and R. A. Buhrman, Spin-torque switching with the giant spin Hall effect of tantalum, Science **336**, 555 (2012).

[4] I. M. Miron, K. Garello, G. Gaudin, P.-J. Zermatten, M. V. Costache, S. Auffret, S. Bandiera, B. Rodmacq, A. Schuhl, and P. Gambardella, Perpendicular switching of a single ferromagnetic layer induced by in-plane current injection, Nature **476**, 189 (2011).

[5] K. Cai, Z. Zhu, J. Lee, R. Mishra, L. Ren, S. D. Pollard, P. He, G. Liang, K. L. Teo, and H. Yang, Ultrafast and energy-efficient spin-orbit torque switching in compensated ferrimagnets, Nat. Electron. **3**, 37 (2020).

[6] M. Cubukcu, O. Boulle, N. Mikuszeit, C. Hamelin, T. Brächer, N. Lamard, M.-C. Cyrille, L. Buda-Prejbeanu, K. Garello, I. M. Miron, *et al.*, Ultrafast perpendicular spin-orbit torque MRAM, IEEE Trans. Magn. **54**, 9300204 (2018).

[7] G. Prenat, K. Jabeur, P. Vanhauwaert, G. D. Pendina, F. Oboril, R. Bishnoi, M. Ebrahimi, N. Lamard, O. Boulle, K. Garello, *et al.*, Ultra-fast and high-reliability SOT-MRAM: From cache replacement to normally-off computing, IEEE Trans. Multi-Scale Comput. Syst. **2**, 1 (2016).

[8] Y. Shiokawa, E. Komura, Y. Ishitani, A. Tsumita, K. Suda, Y. Kakinuma, and T. Sasaki, High write endurance up to 10^{12} cycles in a spin current-type magnetic memory array, AIP Adv. **9**, 035236 (2019).

[9] Y. Cao, G. Xing, H. Lin, N. Zhang, H. Zheng, and K. Wang, Prospect of spin-orbitronic devices and their applications, iScience **23**, 10 (2020).

[10] D. Apalkov, B. Dieny, and J. M. Slaughter, Magnetoresistive random access memory, Proc. IEEE **104**, 10 (2016).

[11] S. Li, S. Goolaup, J. Kwon, F. Luo, W. Gan, and W. S. Lew, Deterministic spin-orbit torque induced magnetization reversal in Pt/$[\mathrm{Co/Ni}]_n$/Co/Ta multilayer Hall bars, Sci. Rep. **7**, 972 (2017).

[12] L. You, R. C. Sousa, S. Bandiera, B. Rodmacq, and B. Dieny, Co/Ni multilayers with perpendicular anisotropy for spintronic device applications, Appl. Phys. Lett. **100**, 172411 (2012).

[13] L. Liu, J. Yu, R. González-Hernández, C. Li, J. Deng, W. Lin, C. Zhou, T. Zhou, J. Zhou, H. Wang, *et al.*, Electrical switching of perpendicular magnetization in a single ferromagnetic layer, Phys. Rev. B. **101**, 220402 (2020).

[14] M. Tang, K. Shen, S. Xu, H. Yang, S. Hu, W. Lü, C. Li, M. Li, Z. Yuan, S. J. Pennycook, *et al.*, Bulk spin torque-driven perpendicular magnetization switching in $L1_0$ FePt single layer, Adv. Mater. **32**, 2002607 (2020).

[15] S. Q. Zheng, K. K. Meng, Q. B. Liu, J. K. Chen, J. Miao, X. G. Xu, and Y. Jiang, Disorder dependent spin-orbit torques in $L1_0$ FePt single layer, Appl. Phys. Lett. **117**, 242403 (2020).

[16] G. Yu, P. Upadhyaya, Y. Fan, J. G. Alzate, W. Jiang, K. L. Wong, S. Takei, S. A. Bender, L.-T. Chang, Y. Jiang, *et al.*, Switching of perpendicular magnetization by spin-orbit torques in the absence of external magnetic fields, Nat. Nanotechnol. **9**, 548 (2014).

[17] L. You, O. Lee, D. Bhowmik, D. Labanowski, J. Hong, J. Bokor, and S. Salahuddin, Switching of perpendicularly polarized nanomagnets with spin orbit torque without an external magnetic field by engineering a tilted anisotropy, Proc. Natl. Acad. Sci. U. S. A. **112**, 10310 (2015).

[18] Y.-W. Oh, S. C. Baek, Y. M. Kim, H. Y. Lee, K.-D. Lee, C.-G. Yang, E.-S. Park, K.-S. Lee, K.-W. Kim, G. Go, *et al.*, Field-free switching of perpendicular magnetization through spin-orbit torque in antiferromagnet/ferromagnet/oxide structures, Nat. Nanotechnol. **11**, 878 (2016).

[19] K. Cai, M. Yang, H. Ju, S. Wang, Y. Ji, B. Li, K. W. Edmonds, Y. Sheng, B. Zhang, N. Zhang, *et al.*, Electric field control of deterministic current-induced magnetization switching in a hybrid ferromagnetic/ferroelectric structure, Nat. Mater. **16**, 712 (2017).

[20] Z. Zhao, A. K. Smith, M. Jamali, and J.-P. Wang, External-field-free spin Hall switching of perpendicular magnetic nanopillar with a dipole-coupled composite structure, Adv. Electron. Mater. **6**, 1901368 (2020).

[21] Y.-C. Lau, D. Betto, Karsten Rode, J. M. D. Coey, and Plamen Stamenov, Spin-orbit torque switching without an external field using interlayer exchange coupling, Nat. Nanotechnol. **11**, 758 (2016).

[22] Y. Sheng, K. W. Edmonds, X. Ma, H. Zheng, and K. Wang, Adjustable current-induced magnetization switching utilizing interlayer exchange coupling, Adv. Electron. Mater. **4**, 1800224 (2018).

[23] X. Wang, C. Wan, W. Kong, X. Zhang, Y. Xing, C. Fang, B. Tao, W. Yang, L. Huang, H. Wu, *et al.*, Field-Free programmable spin logics via chirality-reversible spin-orbit torque switching, Adv. Mater. **30**, 1801318 (2018).

[24] X. Xie, X. Zhao, Y. Dong, X. Qu, K. Zheng, X. Han, X. Han, Y. Fan, L. Bai, Y. Chen, *et al.*, Controllable field-free switching of perpendicular magnetization through bulk spin-orbit torque in symmetry-broken ferromagnetic films, Nat. Commun. **12**, 2473 (2021).

[25] See the Supplemental Material at http://link.aps.org/supplemental/10.1103/PhysRevApplied.19.024034 for switching at low temperature, planar hall effect measurement, harmonic measurements of single FePt and FePt(5)/TiN(3.5)/NiFe(15), and thermal effects during the electrical measurements.

[26] S. O. Demokritov, C. Bayer, S. Poppe, M. Rickart, J. Fassbender, B. Hillebrands, D. I. Kholin, N. M. Kreines, and O. M. Liedke, Control of Interlayer Exchange Coupling in Fe/Cr/Fe Trilayers by Ion Beam Irradiation, Phys. Rev. Lett. **90**, 097201 (2003).

[27] R. P. Erikson, K. B. Hathaway, and J. R. Cullen, Mechanism for non-Heisenberg-exchange coupling between ferromagnetic layers, Phys. Rev. B. **47**, 2626 (1993).

[28] K. F. Dong, Y. Y. Jiao, Z. Y. Yuan, C. Sun, K. H. He, F. Jin, W. Q. Mo, and J. L. Song, Low magnetic damping of epitaxial NiFe (100) thin films grown on different substrate, J. Magn. Magn. Mater. **523**, 167615 (2021).

[29] S. S. P. Parkin, R. Bhadra, and K. P. Roche, Oscillatory Magnetic Exchange Coupling through Thin Copper Layers, Phys. Rev. Lett. **66**, 2152 (1991).

[30] M. Hayashi, J. Kim, M. Yamanouchi, and H. Ohno, Quantitative characterization of the spin-orbit torque using harmonic Hall voltage measurements, Phys. Rev. B. **89**, 144425 (2014).

[31] S. Fukami, C. Zhang, S. DuttaGupta, A. Kurenkov, and H. Ohno, Magnetization switching by spin–orbit torque in an antiferromagnet–ferromagnet bilayer system, Nat. Mater. **15**, 535 (2016).

[32] J. Grollier, D. Querlioz, K. Y. Camsari, K. Everschor-Sitte, S. Fukami, and M. D. Stiles, Neuromorphic spintronics, Nat. Electron. **3**, 360 (2020).

[33] S. Zhang, *et al.*, A spin-orbit-torque memristive device, Adv. Electron. Mater. **5**, 1800782 (2019).

[34] Y. Cao, A. W. Rushforth, Y. Sheng, H. Zheng, and K. Wang, Tuning a binary ferromagnet into a multistate synapse with spin-orbit-torque-induced plasticity, Adv. Funct. Mater. **29**, 1808104 (2019).

[35] J. Yun, Q. Bai, Z. Yan, M. Chang, J. Mao, Y. Zuo, D. Yang, Li Xi, and D. Xue, Tailoring multilevel-stable remanence states in exchange biased system through spin-orbit torque, Adv. Funct. Mater. **30**, 1909092 (2020).

[36] J. Zhou, T. Zhao, X. Shu, L. Liu, W. Lin, S. Chen, S. Shi, X. Yan, X. Liu, and J. Chen, Spin-orbit torque-induced domain nucleation for neuromorphic computing, Adv. Mater. **33**, 2103672 (2021).

[37] P. Bruno, Oscillations of interlayer exchange coupling vs. ferromagnetic-layers thickness, Europhys. Lett. **23**, 8 (1993).

[38] P. J. H. Bloemen, M. T. Johnson, M. T. H. van de Vorst, R. Coehoorn, J. J. de Vries, R. Jungblut, J. aan de Stegge, A. Reinders, and W. J. M. de Jonge, Magnetic Layer Thickness Dependence of the Interlayer Exchange Coupling in (001) Co/Cu/Co, Phys. Rev. Lett. **72**, 764 (1994).